

Impact of an Ionic Liquid Solution on Horseradish Peroxidase Activity

Shubham Chatterjee, Jorge Nochebuena, and G. Andrés Cisneros*



Cite This: *J. Am. Chem. Soc.* 2024, 146, 13247–13257



Read Online

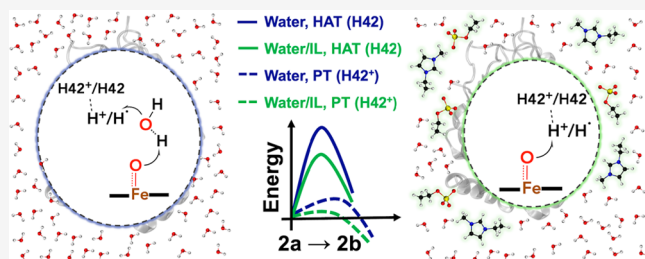
ACCESS |

Metrics & More

Article Recommendations

Supporting Information

ABSTRACT: Horseradish peroxidase (HRP) is an enzyme that oxidizes pollutants from wastewater. A previous report indicated that peroxidases can have an enhancement in initial enzymatic activity in an aqueous solution of 0.26 M 1-ethyl-3-methylimidazolium ethyl sulfate ($[EMIm][EtSO_4]$) at neutral pH. However, the atomistic details remain elusive. In the enzymatic landscape of HRP, compound II (Cpd II) plays a key role and involves a histidine (H42) residue. Cpd II exists as oxoferryl (2a) or hydroxoferryl (2b(Fe^{IV})) forms, where 2a is the predominantly observed form in experimental studies. Intriguingly, the ferric 2b(Fe^{III}) form seen in synthetic complexes has not been observed in HRP. Here, we have investigated the structure and dynamics of HRP in pure water and aqueous $[EMIm][EtSO_4]$ (0.26 M), as well as the reaction mechanism of 2a to 2b conversion using polarizable molecular dynamics (MD) simulations and quantum mechanics/molecular mechanics (QM/MM) calculations. When HRP is solvated in aq $[EMIm][EtSO_4]$, the catalytic water displaces, and H42 directly orients over the ferryl moiety, allowing a direct proton transfer (PT) with a significant energy barrier reduction. Conversely, in neat water, the reaction of 2a to 2b follows the previously reported mechanism. We further investigated the deprotonated form of H42. Analysis of the electric fields at the active site indicates that the aq $[EMIm][EtSO_4]$ medium facilitates the reaction by providing a more favorable environment compared with the system solvated in neat water. Overall, the atomic level supports the previous experimental observations and underscores the importance of favorable electric fields in the active site to promote catalysis.



INTRODUCTION

Horseradish peroxidase (HRP) is a heme-based enzyme obtained from the roots of the horseradish plant (*Armoracia rusticana*). HRP is an important biotechnological enzyme because it catalyzes the oxidation of various phenols from polluted wastewater, in the presence of hydrogen peroxide to form oligomeric and polymeric products.^{1–5} The active site of HRP (PDB code 1HCH)¹⁰⁴ consists of a heme prosthetic group, which is the locus of enzymatic activity. In the active site, the iron ion held within heme's porphyrin ring structure is the key catalytic element. The active site in HRP includes three catalytically important residues, H42, H170, a second-shell R38 that contribute to substrate binding and orientation, and an ordered water molecule over the ferryl moiety (Figure 1a). R38 is a conserved residue;⁶ it facilitates the binding of H_2O_2 to HRP and helps cleave the O–O bond of the peroxide, stabilizing the transition state intermediate for the formation of compound I from the resting state.^{6–8} Mutagenesis (R38L⁶ and H42E:R38S⁹) studies have shown a decrease in the formation of compound I in the absence of R38. The iron cation at the center of the heme cofactor transitions between different oxidation states during the catalytic cycle, enabling the enzyme to engage in electron transfer reactions (Figure 1b).

Initially, HRP exists in a resting state with iron in a ferric configuration (Fe^{III}) (Figure 1b). Binding of H_2O_2 oxidizes iron

to a +4 oxidation state resulting in the formation of compound I (Cpd I), and reducing H_2O_2 to water. Next, Cpd I engages with the substrate via a redox reaction, where one electron is transferred from the substrate to the heme complex, resulting in the formation of compound II (Cpd II). In the last step of the catalytic cycle, Cpd II oxidizes a substrate molecule with the formation of the original resting state for the subsequent catalytic cycles.^{10–12}

A study using spectrophotometry indicated that the conversion of Cpd II back to its resting state is the slowest, and therefore the rate limiting step, in the process of oxygen production by HRP.¹³ The rate constant for HRP catalysis at pH 6.0 when incubated solely with H_2O_2 , is reported as $1.78 \pm 0.12 s^{-1}$ ¹⁴ equivalent to an estimated activation energy barrier (ΔG^\ddagger) of 17.1 kcal mol⁻¹.^{15,16}

In the enzymatic landscape of HRP, Cpd II presents an interesting case of structural versatility. Previous experimental

Received: January 25, 2024

Revised: April 27, 2024

Accepted: April 29, 2024

Published: May 3, 2024



ACS Publications

© 2024 American Chemical Society

13247

<https://doi.org/10.1021/jacs.4c01100>

J. Am. Chem. Soc. 2024, 146, 13247–13257

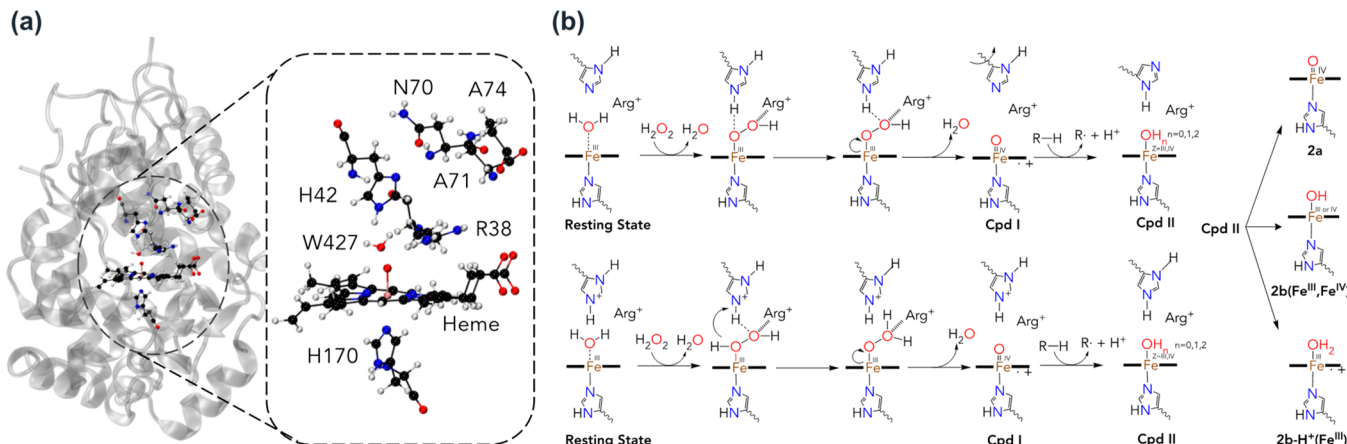


Figure 1. Active site of HRP Compound I (PDB code 1HCH) and selected nearby surface residues. (b) Proposed HRP catalysis (top, neutral pH (H42); bottom, acid pH (H42⁺)).

studies¹⁷ suggest that in the active site of HRP Cpd II can coexist as oxoferryl (2a) and hydroxoferryl (2b(Fe^{IV})) forms. Intriguingly, the ferric form of 2b, i.e., 2b(Fe^{III}), has never been detected or reported in HRP.

This absence is contrasted by the predominance of the 2a form among synthetic Cpd II species.^{18–39} A theoretical study by Derat et al. suggested 2b-H⁺(Fe^{III}) as a possible alternative form of Cpd II, although there has not been an experimental report for this form in HRP.¹⁰ This computational work, based on the unrelaxed crystal structure solvated in pure water, using a protonated H42 and a modified porphyrin ring, explored the proton transfer reaction from protonated H42 (referred here as H42⁺) to the FeO moiety in HRP's active site resulting in a calculated reaction barrier of 0.71 kcal mol⁻¹. The proposed ionization state of H42 was based on the possibility that HRP is active under acidic pH conditions, or a postulated scenario under neutral pH where a proton is transferred to H42 in a previous step.¹⁰

Room-temperature ionic liquids (RTILs), known for their adjustable properties, can act as environmentally friendly substitutes for conventional organic solvents in biocatalysis, including peroxidases.^{40–42} These organic salts, liquid near room temperature, have been reported to offer advantages in enzymatic catalysis such as improvements in activity and stability.^{3,40–43} A previous experimental study³ by Carneiro et al. showed that a commercial peroxidase (E.C. 1.11.1.7) demonstrated enhanced initial activity when solvated in room temperature ionic liquids (RTILs) under specific conditions of pH and IL concentration. In particular, the optimal enzyme activity was observed at neutral pH and when the concentration of ILs ranged from 5% (corresponding to 0.26 M) to 10% v/v. Among the two ionic liquids (ILs) examined, [EMIm][EtSO₄] was reported to be the most favorable IL for maintaining peroxidase activity.

The presence of the 2a and 2b(Fe^{IV}) forms in the active site of HRP with 2a being the predominant species, coupled with the absence of the 2b(Fe^{III}) form in HRP despite its presence in synthetic complexes, raises questions about the relative stability of 2a and 2b forms of Cpd II and possible conversion of 2a to 2b (Fe^{III/IV}). Furthermore, the involvement of Cpd II in the rate-determining step for oxygen production by HRP necessitates further investigation into its various oxidation states. Additionally, given the fact that a commercial peroxidase showed higher activity in aq [EMIm][EtSO₄], investigating the conversion of

2a to 2b(Fe^{III}) and 2b(Fe^{IV}) in neat water and in aq [EMIm][EtSO₄] may uncover features that remain unresolved and illustrate the impact of the solvent environment on HRP catalysis.

In the present work, we present the computational investigation of the impact of the solvent environment on HRP catalysis for reactions based on Cpd II with H42⁺ and H42 in two solvents, namely, water and 5% (v/v) aq [EMIm][EtSO₄] with relaxed structure of HRP. The organization of the paper is as follows: the next section describes the details of molecular dynamics (MD) simulations followed by QM/MM calculations, with the polarizable AMOEBA (atomic multipole optimized energetics for biomolecular applications)^{44–48} force field (FF). Subsequently, we present the results of the comparative structural and dynamical analysis between for HRP in the two solvents, resulting catalytic mechanism, and electronic analysis along the reaction path, followed by concluding remarks.

■ COMPUTATIONAL APPROACH

The initial coordinates for horseradish peroxidase in compound I state were obtained from the RCSB Protein Data Bank (PDB code 1HCH). The standard protonation forms at pH = 7 of all titratable amino acid residues in the protein were determined using propKa.^{49,50} Four systems have been considered including neat water systems with H42 and H42⁺, referred to as Water(H42) and Water(H42⁺), respectively, and 5% (v/v) aq [EMIm][EtSO₄] systems with H42 and H42⁺ are referred to as Water/IL(H42) and Water/IL(H42⁺), respectively.

For H42, situated at the active site and positioned above the heme group, we chose the ϵ protonation state. We assume that the H42 residue could orient itself to facilitate the transfer of the hydrogen atom to the ordered water molecule. For H170, which is axially ligated to iron, we selected the δ protonation state to ensure coordination with the iron. The all-atom AMOEBA polarizable force field^{44,45} was employed to simulate standard protein residues, water molecules, and counterions. The parameters for water molecules and the protein residues were obtained from the AMOEBA-PROTEIN-2013 force-field library.⁴⁵ Parameters of IL ions were obtained from the AMOEBA-IL FF.⁵¹ Parameters for the heme b prosthetic group and oxygen atom in FeO moiety were acquired with TINKER8⁵⁴ and GDMA 2.3.⁵² All of the newly created parameters are included in Supporting Information.

For the Water(H42) system the crystal structure was solvated with 10 638 water molecules immersed in a periodic unit cell of dimensions 70^3 \AA^3 . For the Water/IL(H42) system we created a cubic box of 72^3 \AA^3 , comprising 10 638 water molecules and 60 [EMIM][EtSO₄] ion pairs. PACKMOL⁵³ was used to build the unit cells for both systems. Each system was neutralized with potassium counterions. In both systems, we considered a minimum distance of 10 Å between the edge of the HRP and the edge of the box.

Both systems were minimized using the BFGS algorithm with a convergence criterion (RMS gradient) of 0.1 Å. After minimization, the systems were equilibrated for 3 ns, incrementing the temperature by 50 K every 500 ps from 0 to 300 K. At this point, the protein was retrained using a force constant of 100.0 kcal Å⁻², and only solvent molecules and counterions were allowed to move freely. Next, at 300 K, the restraints on the protein were reduced from 100 kcal Å⁻² in steps of 25 kcal Å⁻² for 500 ps at each step until no restraints remained. Then an MD (of 2 ns) was performed to reach consistent cell parameters. Finally, a 30 ns MD simulation was performed using the Tinker8⁵⁴ code. We ran three replicas for each system, resulting in 90 ns total MD, taking the last 20 ns of each replica as the production portion of the ensemble (60 ns total production for each system). All simulations were conducted under isothermal–isobaric (*NPT*) conditions, employing an integration time step of 1 fs. van der Waals and electrostatic interactions were calculated by using a 9 Å cutoff at each time step. Periodic boundary conditions were applied. Long-range Coulomb interactions were treated using the smooth particle mesh Ewald^{55–57} (PME) algorithm, while the isotropic smoothing method was used for van der Waals.⁵⁸ Temperature and pressure at 300 K and 1 bar were maintained via the Bussi thermostat⁵⁹ and Berendsen barostat,⁶⁰ respectively. VMD⁶¹ was utilized to visualize, analyze, and generate all images.

After the MD simulations, root mean square deviation (RMSD) and root mean square fluctuations (RMSF) were calculated with VMD and MDAnalysis,^{62,63} respectively. Energy decomposition analysis (EDA) was carried out with 250 frames from the MD simulation using the analyze utility in Tinker. To study the diffusion of EtSO₄⁻ ions, we computed the site–site radial pair distribution function (RDF, $g(r)$) and spatial distribution function (SDF) of these ions with TRAVIS.^{64–67} All atoms of EtSO₄⁻ were considered for $g(r)$ and SDF calculations as a function of distance from residues N70, A71, and A74 as references to a maximum radius of 15 Å.

Representative structures were selected from the production trajectories to obtain the reactant and product structures for subsequent QM/MM calculations. Selected representatives for the QM/MM calculations were obtained via the *k*-means clustering algorithm implemented in Scikit-learn.⁶⁸ The clustering was calculated based on the RMSD of the protein backbone, a random state of 0, a tolerance of 0.0001, and a maximum iteration of 500.

All QM/MM calculations were performed using the LICHEM (layered interacting chemical models) QM/MM code^{69–71} by combining Gaussian 16¹⁰⁶ and Tinker 7.^{72–78} The QM subsystem convergences for all QM/MM calculations were as follows: RMS deviation of 0.001 Å, RMS force of 0.03 hartree/bohr, and a maximum force of 0.05 hartree/bohr. The RMS deviation for the MM subsystem was set to 0.3 Å. The QM subsystem includes the porphyrin ring, Fe-atom, oxygen atom of FeO bond, intermediate water molecule (if applicable, see below) between H42 and heme, and H42, H170, and R38

residues. The resulting systems comprise 117 and 114 atoms in the QM region for the Water and Water/IL systems, respectively. All residues, solvent molecules, and ions within a 15 Å sphere of the catalytic Fe in the QM region were selected as active for the MM subsystem optimization, and any fragment outside this region was held static.

Reactant and product systems were optimized using the Davidon–Fletcher–Powell (DFP) algorithm.^{79,80} The pair of reactant and product structures that yielded either exothermic or slightly endothermic reaction energies were selected as end points for calculating the minimum energy path (MEP) of the reaction occurring within the active site. Reaction path optimizations were performed with the quadratic string method (QSM).⁸¹ Initially, we employed the restrained molecular mechanics (MM) method with a force constant of 10 kcal mol⁻¹ Å⁻². After each major cycle, the force constant on the MM environment atoms was halved until no restraints on the MM region remained. QM/MM optimizations were carried out using the unrestricted Kohn–Sham formalism, employing the UPBEO functional^{82–84} and the 6-31G(d) basis set^{85–87} for all atoms except for Fe, which was described with the def2-SVP basis set.⁸⁸ Previously, this methodology has been employed for the analysis of protoporphyrins.⁸⁹ The MM environment was represented by using the polarizable AMOEBA force field. The pseudobond approach was utilized to handle covalent bonds spanning the QM/MM boundary.^{90–94} Single-point calculations on all of the optimized critical points were performed at the ωB97X-D/6-311+G(d,p)//AMOEBA level. Long-range electrostatic effects for all QM/MM calculations were accounted for via the QM/MM long-range electrostatic correction (QM/MM-LREC)^{95,96} for QM coupled with the smooth particle mesh Ewald (sPME) for the MM utilizing a cutoff of 25 Å. The calculations for the MM subsystem were conducted by using the smooth particle mesh Ewald (sPME) method under periodic boundary conditions.

For studying the reaction mechanism in Water(H42⁺) and Water/IL(H42⁺) systems, the reactants were obtained by protonating H42 and optimizing the reactants of Water(H42) and Water/IL(H42) to get the reactants for Water(H42⁺) and Water/IL(H42⁺) systems, respectively. A short MD simulation (0.50 ns) was carried on with these reactants to relax the systems. A representative was obtained from this simulation for subsequent QM/MM calculations.

We employed the Multiwfn 3.8 software⁹⁷ to compute noncovalent interactions within the QM region. Noncovalent Interaction (NCI) analysis, also known as reduced density gradient (RDG) analysis, is widely used for studying weak interactions.^{98–103} NCI regions are identified as areas with low density and a low reduced gradient. We computed NCI regions using a high-quality grid and employed the standard RGB color scheme: red, green, and blue regions correspond to repulsive, weak, and attractive interactions, respectively. Electron localization function (ELF)^{104,105} analysis including basin population and dipole moment analyses was also performed with Multiwfn 3.8. For our analyses, we obtained the wave functions for the QM region in both the presence (QM/MM) and absence of the MM region (QM-only) using Gaussian 16, enabling the investigation of environmental effects. Mulliken spin density calculations and spin localized orbital bonding analysis (LOBA)¹⁰⁶ at the ωB97X-D^{107,108}/6-311+g(d,p)//AMOEBA level were carried out with Multiwfn. We investigated the triplet and singlet spin states of 2a and 2b and found the triplet states to be the ground electronic states (Table S2).

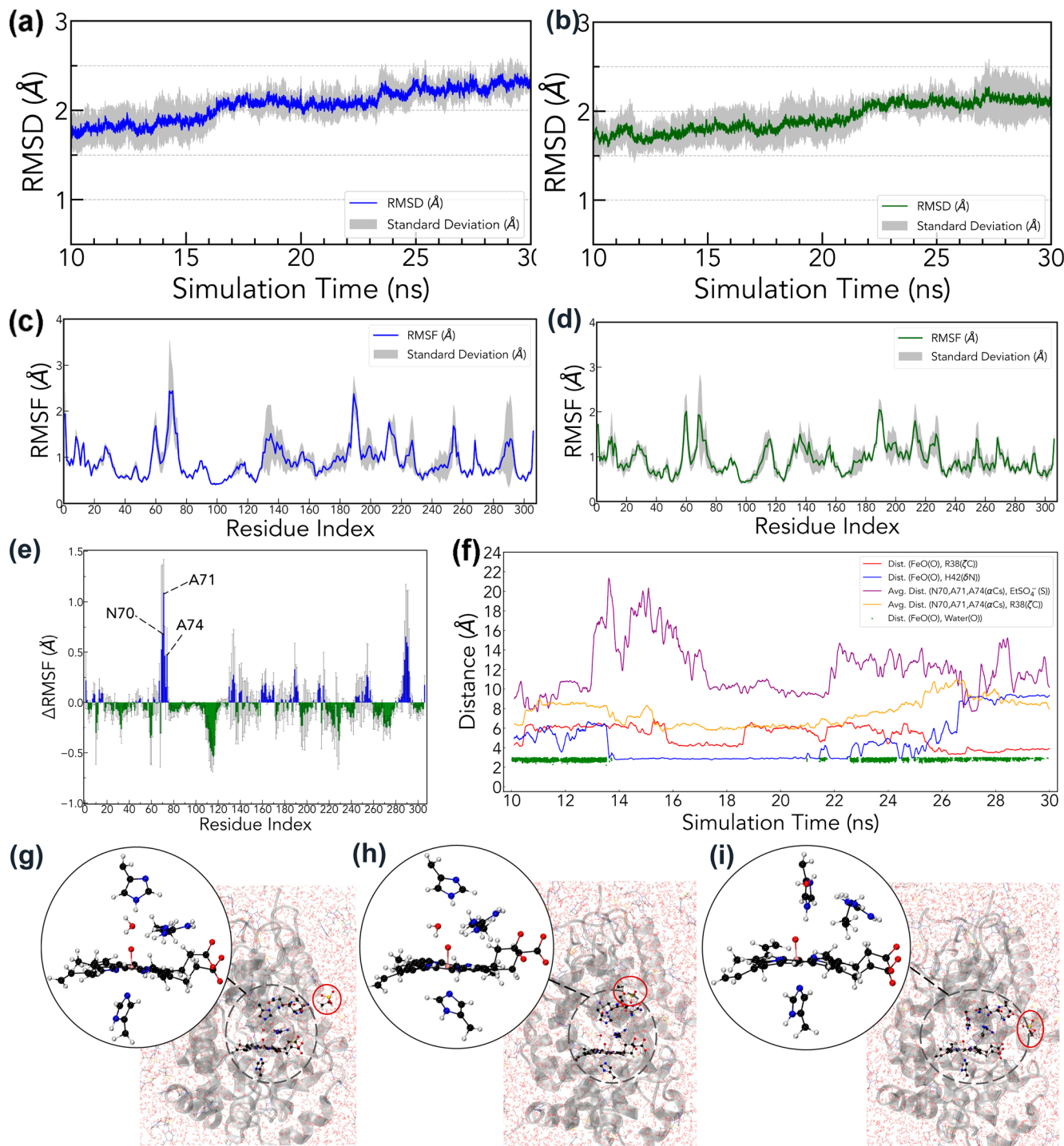


Figure 2. (a) and (b) show the averaged RMSD plots corresponding to Water(H42) and Water/IL(H42) systems, respectively. (c, d) Averaged RMSF of the residues during the production in three replicas in Water(H42) and Water/IL(H42) systems, respectively. (e) Plot of the difference in average residual RMSF (Δ RMSF) in Water(H42) and Water/IL(H42) systems. A positive value of Δ RMSF corresponds to higher residual fluctuations in Water(H42) system, and a negative value corresponds to higher residual fluctuations in Water/IL(H42) system. (f) Changes in selected distances with respect to simulation time in one of the replicas of the Water/IL(H42) system. The discontinuities in the distances are due to the exchange of one water molecule with another water molecule and the absence of a water molecule between H42 and ferryl moiety. Representative structures with magnified images of the active site for the initial (g), intermediate (h), and final (i) stages of the simulation. Residues shown in balls and sticks correspond to the heme group, ordered water, R38, N70, A71, A74, and an EtSO_4^- ion migrating toward the protein. The EtSO_4^- ion is encircled in a red color.

RESULTS AND DISCUSSION

RMSD (Figure 2a,b) and RMSF analyses (Figure 2c,d) were performed to analyze the structure of HRP during the MD simulations. Figure 2e shows that the Water/IL solvent results in a significant change in the root mean squared fluctuation.

Specifically, several residues show higher fluctuations in the Water(H42) system compared with the IL/water solvated HRP. These results suggest that the Water/IL(H42) medium dampens the motion of these residues. Interestingly, a specific region comprising residues N70, A71, and A74 shows the largest

decrease in fluctuations in the Water/IL(H42) system compared with Water(H42) (Figure 2e). The reduction in fluctuation of these three specific residues suggests differences in the protein at these sites between the Water(H42) and Water/IL(H42) systems. Given that the only difference between these systems is the presence of the IL ions, we performed structural, radial, and structure distribution function analyses of the ions around these residues to investigate the impact of the IL on the protein structure at these positions.

In the initial stages of the simulation (Figure 2g), EtSO_4^- ions are randomly distributed in the solvent. Around 3 ns, EtSO_4^- ions get closer to N70, A71, and A74, with a concomitant shift of R38 toward these residues from the opposite side (Figure 2h). As the simulation progresses, the distance between EtSO_4^- ions and N70, A71, and A74 is reduced (Figure 2i), with R38 getting everted from the active site. The proximity of the anions to these three residues results in direct interactions that lower the RMSF values of these specific residues in the Water/IL(H42) system. In the initial stages of MD simulation (Figure 2g) in the Water/IL(H42) system, the active site of HRP retains the water molecule in the active site between H42 and the FeO moiety. However, the shift of R38 away from the active site results in the unbinding of the water molecule from the FeO moiety (Figure 2f).

The interaction energy between the water molecule in the active site and R38 is $-5.4 \text{ kcal mol}^{-1}$. The shift of R38 away from the active site breaks two H-bonds with the ordered water molecule, and subsequently, around 4.2 ns, the water molecule migrates out of the active site. Subsequently, H42 moves closer to the ferryl moiety, which could facilitate the transfer from H42 to the heme. R38 is situated close ($<10 \text{ \AA}$) to N70, A71, and A74. As explained in the Introduction, R38 plays a significant role in catalysis and is highly conserved (Figure S9). EDA reveals an interaction energy of $-12.9 \text{ kcal mol}^{-1}$ between R38 and the EtSO_4^- ion located near these surface residues (Figure 2i). Between 10 and 13 ns, H42 migrates away from the heme (Figure 2f) while the ordered water molecule is still located in the active site. Eventually at around 13 ns the water molecule migrates out of the active site, and subsequently H42 shifts closer to heme. This configuration of the active site is dynamic. A water molecule could enter the active site and momentarily reside between H42 and the ferryl moiety (Figure S7).

RDF analysis of EtSO_4^- ions with respect to N70, A71, and A74 (Figure 3a–c) shows peaks around 11.2, 10.2, and 6.8 Å, respectively, for Water/IL(H42) system. Additionally, significant SDF surfaces were observed near these residues, as shown in Figure 3d–f. These RDF and SDF results support the observation of the migration of EtSO_4^- ions to the vicinity of these surface residues.

Following the MD simulations, a clustering analysis was employed to select representatives for subsequent QM/MM calculations. The trends selected for *k*-means clustering include the distance between the O atom of FeO moiety and δN of H42. In the Water/IL(H42), the shift of R38 away from the active site resulted in significant changes in the active site; thus, we selected the distance between the O atom of the ferryl moiety and ζC of R38 as the second trend for clustering. Based on the two trends, we used the elbow-method (Figure S5) to get the optimal number of clusters. We identified two and four clusters for the Water(H42) and Water/IL(H42) systems, respectively, as shown in Figure 4.

The criteria used herein to determine catalytically competent systems involve distances for the atom abstraction from H42 and

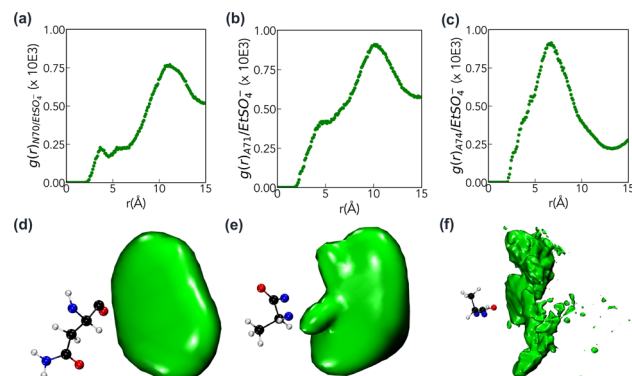


Figure 3. Radial distribution function (RDF) and spatial distribution function (SDF) analysis of EtSO_4^- ions with respect to N70(a), A71(b), and A74(c), respectively. Panels d, e, and f show the SDF of EtSO_4^- ions in the vicinity of N70, A71, and A74, respectively (isovalue = 1.0 and maximum observation radius = 15 Å).

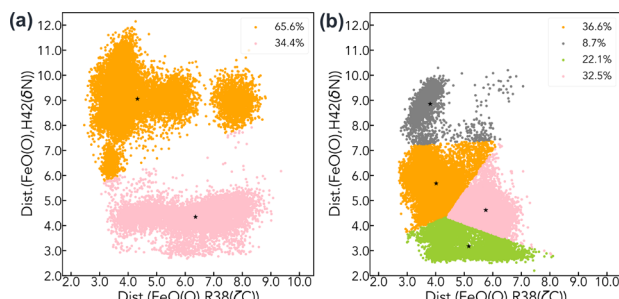


Figure 4. *k*-mean values analysis for the Water(H42) (a) and Water/IL(H42) (b) systems, respectively.

subsequent transfer via the ordered water (for the Water systems) or direct transfer (for Water/IL systems) with values of $<5.0 \text{ \AA}$ between the O atom of FeO moiety and δN of H42, and values of $<3.5 \text{ \AA}$ for Water/IL system. Based on these criteria, several suitable reactant representatives for further QM/MM studies were selected from the catalytically competent clusters in both mediums (pink cluster for Water and green and pink clusters for Water/IL system). These representatives were optimized via QM/MM methodology, and for each of these optimized reactants, products were generated in silico and optimized. The optimized reactant and product pair that resulted in the lowest reaction energy (MEP) were used as end points to calculate the minimum energy paths associated with the reported HAT reactions (Tables S16 and S17).

Parts a, b, c, and d of Figure S4 show the noncovalent interactions for the reactant systems of Water(H42 $^+$), Water/IL(H42 $^+$), Water(H42), and Water/IL(H42), respectively. For the water-solvated systems, an H-bond is observed between H42 and the ordered water molecule, and another H-bond (in the case of Water(H42)), between the water molecule and FeO moiety. Furthermore, two NCI surfaces between R38 and the water molecule reveal weak attractive interactions between R38 and the water molecule. Attractive interactions with H42, ferryl, and R38 enhance the stability of the ordered water in the active site. Conversely, for the aq IL-solvated systems, the ordered water no longer remains in the active site, and instead a direct hydrogen-bond interaction is observed between the H atom on H42 and the ferryl moiety for both Water/IL(H42 $^+$) and Water/IL(H42) systems. The formation of this direct contact between H42 and the ferryl is a consequence of the rearrangement of R38

in response to the approach of EtSO_4^- ions to residues 70–74 (Figure 3), which results in the migration of the water molecule away from the active site, as described above.

The optimized paths for the four different systems suggest two possible mechanisms: a water-mediated reaction for the Water($\text{H}42^+$) and Water($\text{H}42$) systems, or direct transfer for the Water/IL($\text{H}42^+$) and Water/IL($\text{H}42$) systems (Figure 5a).

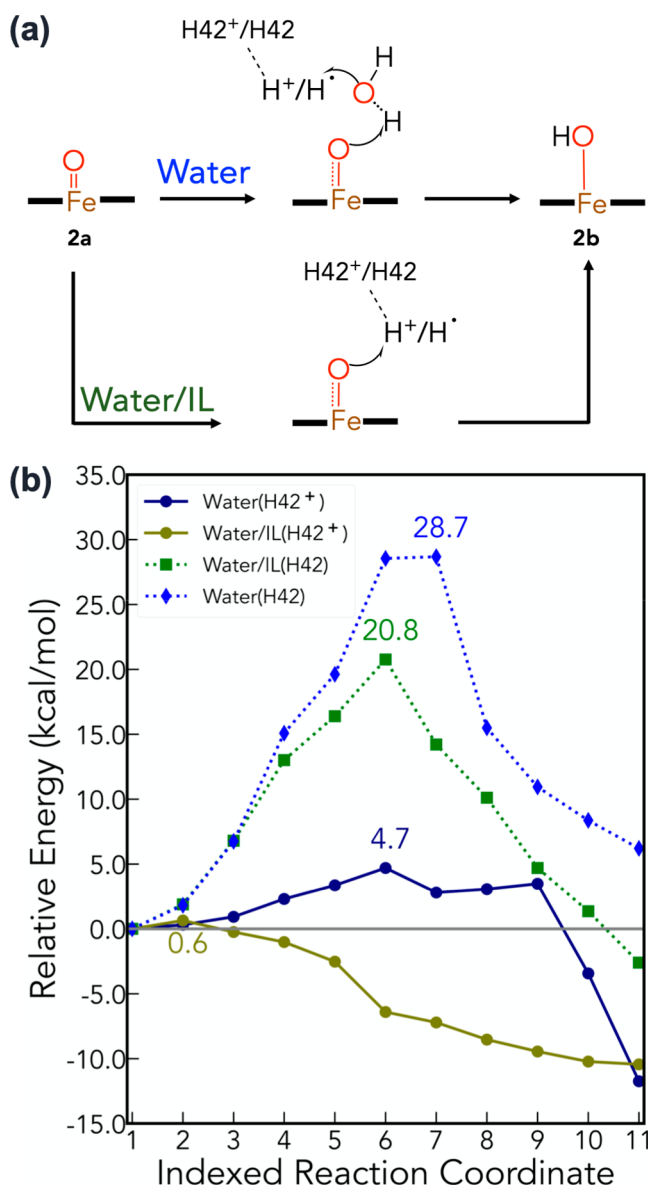


Figure 5. (a) Reaction mechanism schemes for the Water and Water-IL solvated systems. (b) Calculated QM/MM reaction paths for reactions 2a to 2b for Water($\text{H}42^+$), Water/IL($\text{H}42^+$), Water($\text{H}42$), and Water/IL($\text{H}42$) systems.

The calculated minimum energy paths for MEPs for all four systems are shown in Figure 5b. The calculated reaction energies for the Water($\text{H}42^+$) and Water/IL($\text{H}42^+$) systems are exothermic ($\Delta E = -11.7 \text{ kcal mol}^{-1}$ and $-10.4 \text{ kcal mol}^{-1}$, respectively) with reaction barriers of 4.7 and 0.6 kcal mol^{-1} , respectively. For the neutral H42 systems the calculated reaction barriers (reaction energies) are 28.7(6.2) kcal mol^{-1} and 20.8(-2.6) kcal mol^{-1} for the Water- and Water/IL-solvated systems, respectively. We also performed a QSM optimization

for the Water/IL system starting from a representative that corresponds to the water-mediated mechanism; the calculated path shows this reaction is not feasible due to high exoergicity and high energy barriers (Figure S8).

For the protonated histidine ($\text{H}42^+$) systems, the MEP corresponds to a proton transfer (PT) mechanism regardless of the solvent, whereas the deprotonated system MEPs correspond to a hydrogen atom transfer (HAT) mechanism independent of solvent. Mulliken spin density and ESP charge analysis of the critical points along the QM/MM reaction paths support the hypothesis of two reaction mechanisms (Table S4). Localized orbital bonding analysis (LOBA, Table S5) indicates that the oxidation state of the Fe-atom is +4 in the reactant for both systems and is +3 and +4 for the product in the Water($\text{H}42^+$) and Water/IL($\text{H}42^+$) systems, respectively, suggesting the formation of 2b(Fe^{III}) in Water($\text{H}42^+$) and of 2b(Fe^{IV}) in Water/IL($\text{H}42^+$) respectively from 2a(Fe^{IV}). A previous study by Derat et al. also suggested the formation of a Fe^{III} species for a PT reaction from $\text{H}42^+$ to heme.¹⁰ As described earlier, R38 plays an important catalytic role experimentally; this is also observed in the stabilizing role of R38 for the TS in the Water system, with a stabilizing interaction of -7.46 kcal/mol , which is reduced to -1.03 kcal/mol for the Water/IL system (Table S18).

As mentioned in the Introduction, the 2b(Fe^{III}) species for Cpd II has not been observed experimentally in HRP, although prior computational simulations suggested it may be a possible intermediate based on the calculated low barrier of formation ($0.7 \text{ kcal mol}^{-1}$).¹⁰ In our hands, the corresponding system (Water/ $\text{H}42^+$) has a barrier of $4.7 \text{ kcal mol}^{-1}$. Although this barrier is relatively small, it is non-negligible and could explain the reason for 2b(Fe^{III}) not being observed experimentally for HRP. The difference in calculated barriers between the previous report and the one reported herein is likely due to the difference in simulation protocols including a relaxed protein/solvent system and the use of polarizable FF here, compared with the use of crystal structure coordinates and a nonpolarizable FF previously.¹⁰ Additionally, the large barriers calculated for the neutral H42 systems (regardless of solvent) indicate that the reaction must proceed via protonated $\text{H}42$.

The presence of IL in solution results in a drastic reduction of the calculated barrier, as shown in Figure 5b. These results are consistent with the experimental observation of higher activity of a peroxidase solvated in aq [EMIm][EtSO_4^-] at neutral pH. The effects of the IL are not only due to structural changes as discussed above but also due to changes in the electronic distribution at the active site. An ELF analysis including multipolar decomposition of the electron population on the ELF basins for selected atoms in the active site was conducted on the optimized reactants, products, and approximate TSs for the full QM/MM system and excluding the MM region, referred to as QM-only systems, to determine the effect of the MM environment on the electronic structure of the QM subsystem (Tables S6–S15).

In the Water/IL($\text{H}42^+$) system (Figure 6d–f), the sum of the valence basin dipole moments involving the Fe and oxyl atoms for the QM/MM and QM-only systems between the TS and the reactant is 0.13 ($=|3.89 - 3.73|$) au and 0.22 ($=|3.84 - 3.62|$) au. For the Water($\text{H}42^+$) system (Figure 6a–c) the difference in the QM/MM and QM-only dipole moment sum between the reactant and the TS is 0.38 ($=|4.23 - 3.85|$) au and 0.19 ($=|4.36 - 4.17|$) au, respectively. In addition to the differences in the magnitude of the dipole associated with the electronic

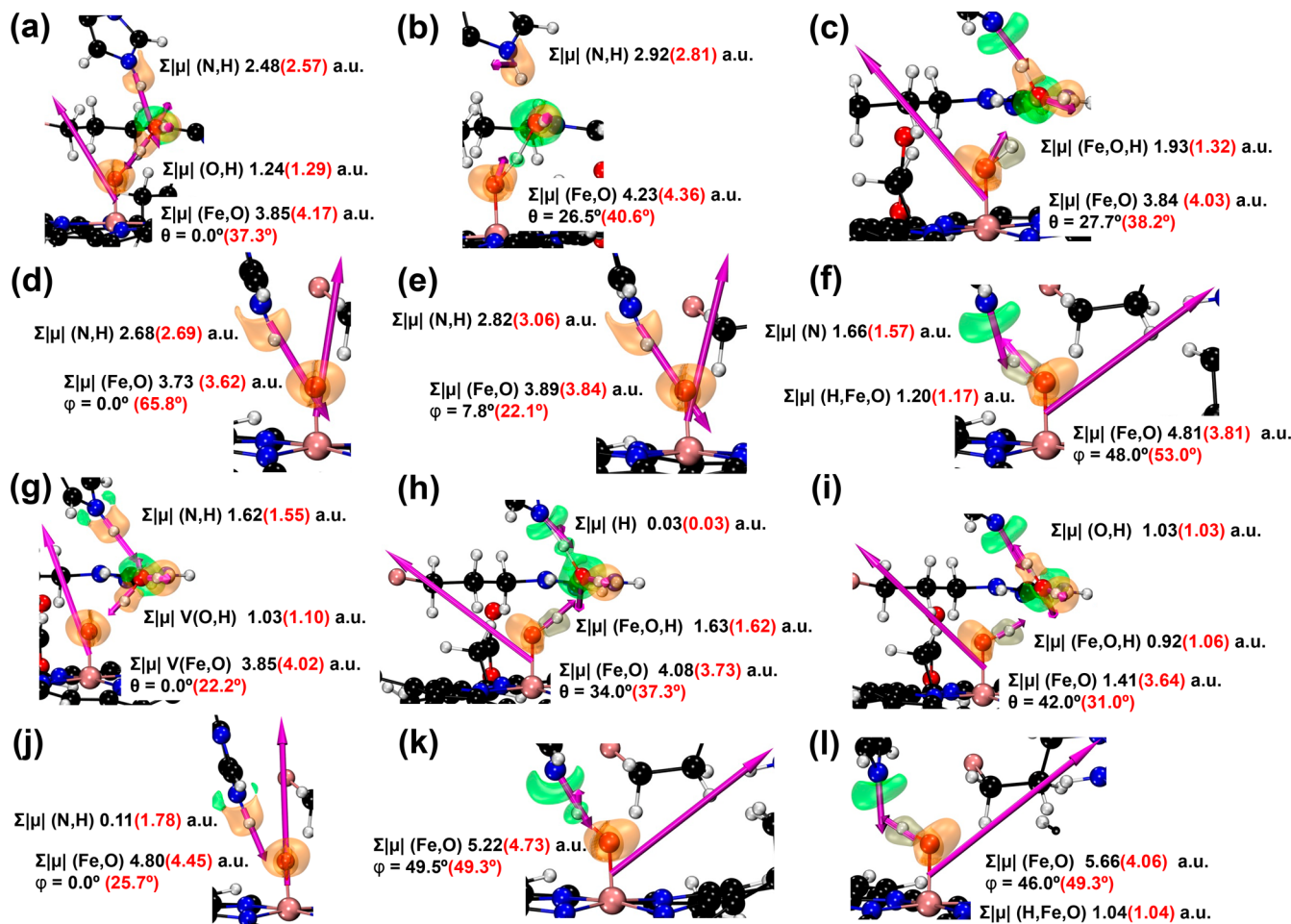


Figure 6. ELF surfaces on the atoms in the active site involved in the catalytic reaction. (a) reactant, (b) TS, (c) product for the Water(H42⁺) system; (d) reactant, (e) TS, (f) product for the Water/IL(H42⁺) system; (g) reactant, (h) TS, (i) product for the Water(H42) system; (j) reactant, (k) TS, (l) product for the Water/IL(H42) system. Monosynaptic ($V(A)$), bisynaptic ($V(A,B)$), and trisynaptic ($V(A,B,C)$) valence basins are shown as green, orange, and tan translucent surfaces. The dipole moment norms of the basins are shown as $\sum|\mu| V(A,B)$. θ and φ are the $V(Fe,O)$ dipole deviations from QM/MM-reactant $V(Fe,O)$ dipoles in Water and Water/IL systems, respectively. The corresponding values of the QM-only cluster counterparts are shown in red. Detailed information about the basins is provided in the Supporting Information.

population of the sum of the basins, the direction of the dipoles (θ/φ) of the FeO basin shows differences as the reaction progresses. In particular from reactant to TS, in the Water(H42⁺) system the QM/MM and QM-only dipole orientation changes by 26.5° (=|26.5° – 0.0°|) and 3.3° (=|40.6° – 37.3°|) compared with 7.8° (=|7.8° – 0.0°|) and 43.7° (=|22.1° – 65.8°|) in the Water/IL(H42⁺) system.

A reduction of the QM/MM FeO basin dipole magnitude and deviation compared to the QM-only systems in the Water/IL(H42⁺) system are observed from the reactant to the TS and indicate a change in the electronic polarization of the Fe–O bond due to the MM environment polarizes in the reactant of the Water/IL(H42⁺) system compared to the Water(H42⁺) system. Similar to the Fe–O bond, we observe a change in the dipole moment associated with N–H bond in the reactants for Water(H42⁺) (2.48 au (Figure 6a)) and Water/IL(H42⁺) (2.68 au (Figure 6d)) systems.

In the case of the Water/IL(H42) and Water(H42) systems, an interesting picture arises that underscores the importance of enzymatic electric fields in the active site and the impact of the solvent on these fields. In the case of the Water(H42) system, a trisynaptic basin comprising the ferryl and transferred H ($V(Fe,O,H)$) is observed for the TS structure, which is absent

in the Water/IL(H42) system. Overall, the difference in the magnitude of the sum of the basin dipoles is not as large between the QM/MM and QM-only systems as the differences observed for the protonated H42 system, although changes are still evident for the reactant and TS structures.

Overall, the comparison of the electron population (Tables S6–S11) and dipoles on the basins associated with the reactive atoms shows the impact of the electric fields around the active site and how even minor changes along the reaction trajectory can result in significant energetic effects on the reaction barrier and reaction energy. In this case, the presence of IL in solution and the close proximity of an ethyl sulfate anion produce both a structural change at the active site and an increase in polarization for the reactant that makes the electric field environment on the reactive atoms more similar to the TS compared with the aqueous only system. This provides a more conducive environment for the reaction that reduces the reaction barrier, helping explain the observed barrier differences for the Water/IL systems regardless of the protonation state of H42.

CONCLUSIONS

In the present study, we compared the effects of neat water and aq [EMIm][EtSO₄] medium on the structure, dynamics, and

catalysis of HRP. Difference RMSF analysis reveals that a small number of amino acids comprising the region between residues 70 and 74 show a large decrease in fluctuation. Radial and structural distribution function analyses show that as the simulation progresses for HRP solvated in aq [EMIm][EtSO₄], EtSO₄ anions approach this region and interact with these residues, reducing their fluctuation. These residues are located on a solvent-exposed α helix that abuts the active site. The EtSO₄ anions around residues 70–74 also show strong nonbonded interactions with R38, inducing a conformational change of R38 away from the active site, which breaks the contacts to the ordered water. For the neat water-solvated system, the ordered water in the active exhibits two hydrogen bonds to R38 and remains ordered when H42 is neutral or protonated. The calculated minimum energy paths associated with the reactions of 2a to 2b follow different reaction mechanisms depending on the ionization state of H42, regardless of the solvent environment. When H42 is positive, the reaction mechanism corresponds to a PT to the ferryl via the ordered water in the neat-water system and directly when HRP is solvated in aq [EMIm][EtSO₄]. Conversely, when H42 is neutral, the reaction mechanism proceeds via a HAT with similar features, i.e., via the ordered water or directly for the neat water and aq [EMIm][EtSO₄] media, respectively. The water-solvated HRP calculated reaction mechanism for H42⁺ is mostly consistent with previous computational simulations. However, a larger reaction barrier is observed presently compared with the previous report, which may help explain the lack of experimental evidence for the 2b(Fe^{III}) species. Interestingly, the calculated barrier when HRP is solvated in aq [EMIm][EtSO₄] is only 0.6 kcal mol⁻¹, which could suggest that 2b(Fe^{IV}) may be able to form and be observed experimentally in this media. The reaction barriers for both PT and HAT reaction mechanisms when HRP is solvated in the IL/water mixture are significantly lower than in neat water. This reduction is due to the structural changes induced by the anions, as well as by a more favorable catalytic environment around the active site. This is evidenced by the favorable polarization of the reactant structures which exhibit electronic dipoles on the reactive atoms/fragments that are significantly closer to those of the TS as obtained from the ELF analysis. Overall, these results indicate that the solvent plays a significant role in enzymatic catalysis, and in the specific case of HRP solvated in IL, the electrostatic environment and structure of the active site are modified resulting in a significant reduction of the reaction barrier. These results are consistent with the experimental observation of higher activity of a peroxidase solvated in aq [EMIm][EtSO₄] at neutral pH.

ASSOCIATED CONTENT

Supporting Information

The Supporting Information is available free of charge at <https://pubs.acs.org/doi/10.1021/jacs.4c01100>.

Newly generated parameters, input coordinates for MD simulations, QM/MM input files, QM/MM reaction paths, and movies corresponding to MEPs ([ZIP](#))

RMSF by residues for Water(H42) and Water/IL(H42), root mean squared fluctuation difference (Δ RMSF) analysis, radial distribution function in Water/IL(H42) system, noncovalent interactions in the active site at the critical points in Water(H42) and Water/IL(H42) systems, elbow plot for k-means clustering, QM/MM energies for singlet and triplet states of the reactant and

products, relative energies corresponding to reaction paths, spin density and ESP charges analysis, LOBA, ELF analysis, and distance analysis for the Water(H42) and Water/IL systems ([PDF](#))

AUTHOR INFORMATION

Corresponding Author

G. Andrés Cisneros — Department of Chemistry and Biochemistry, University of Texas at Dallas, Richardson, Texas 75080, United States; Department of Physics, University of Texas at Dallas, Richardson, Texas 75080, United States; orcid.org/0000-0001-6629-3430; Email: andres@utdallas.edu

Authors

Shubham Chatterjee — Department of Chemistry and Biochemistry, University of Texas at Dallas, Richardson, Texas 75080, United States; orcid.org/0000-0002-5185-8459

Jorge Nochebuena — Department of Physics, University of Texas at Dallas, Richardson, Texas 75080, United States; orcid.org/0000-0003-0707-1066

Complete contact information is available at:

<https://pubs.acs.org/10.1021/jacs.4c01100>

Notes

The authors declare no competing financial interest.

ACKNOWLEDGMENTS

This work was funded by NSF Grant CHE-1856162. Computational time was provided by the University of Texas at Dallas CyberInfrastructure Facilities, and the University of North Texas CASCaM Crunchn3/4 HPC cluster supported by NSF Grant OAC-02117247. Additional computing time from ACCESS Project CHE160044 is gratefully acknowledged.

ABBREVIATIONS

QM/MM, quantum mechanics/molecular mechanics; MD, molecular dynamics; ELF, electron localization function; NCI, noncovalent interaction

REFERENCES

- (1) Conesa, A.; Punt, P. J.; van den Hondel, C. A. M. J. J. Fungal Peroxidases: Molecular Aspects and Applications. *J. Biotechnol.* **2002**, 93 (2), 143–158.
- (2) Husain, Q. Potential Applications of the Oxidoreductive Enzymes in the Decolorization and Detoxification of Textile and Other Synthetic Dyes from Polluted Water: A Review. *Crit. Rev. Biotechnol.* **2006**, 26 (4), 201–221.
- (3) Carneiro, A. P.; Rodríguez, O.; Mota, F. L.; Tavares, A. P. M.; Macedo, E. A. Kinetic and Stability Study of the Peroxidase Inhibition in Ionic Liquids. *Ind. Eng. Chem. Res.* **2009**, 48 (24), 10810–10815.
- (4) Chance, B. The Kinetics of the Enzyme-Substrate Compound of Peroxidase. *Adv. Enzymol. Relat. Areas Mol. Biol.* **1999**, 73 (2), 3–23.
- (5) Penner-Hahn, J. E.; Smith Eble, K.; Dawson, J. H.; Hodgson, K. O. Structural Characterization of High Valent Intermediates in Horseradish Peroxidase. *J. Phys. Colloq.* **1986**, 47 (C8), C8-1137–C8-1142.
- (6) Rodriguez-Lopez, J. N.; Smith, A. T.; Thorneley, R. N. F. Role of Arginine 38 in Horseradish Peroxidase: A CRITICAL RESIDUE FOR SUBSTRATE BINDING AND CATALYSIS (*). *J. Biol. Chem.* **1996**, 271 (8), 4023–4030.
- (7) Derat, E.; Shaik, S. The Poulos-Kraut Mechanism of Compound I Formation in Horseradish Peroxidase: A QM/MM Study. *J. Phys. Chem. B* **2006**, 110 (21), 10526–10533.

- (8) Al-Fartusie, F. S. D. Engineering and Characterisation of Novel Protein Covalent Linkages in Horseradish Peroxidase (HRP): Effect on Structure and Function. Ph.D. Thesis, University of Sussex, Brighton, U.K., 2011.
- (9) Meno, K.; Jennings, S.; Smith, A. T.; Henriksen, A.; Gajhede, M. Structural Analysis of the Two Horseradish Peroxidase Catalytic Residue Variants H42E and R38S/H42E: Implications for the Catalytic Cycle. *Acta Crystallogr., Sect. D: Biol. Crystallogr.* **2002**, *58* (10), 1803–1812.
- (10) Derat, E.; Shaik, S. Two-State Reactivity, Electromerism, Tautomerism, and “Surprise” Isomers in the Formation of Compound II of the Enzyme Horseradish Peroxidase from the Principal Species, Compound I. *J. Am. Chem. Soc.* **2006**, *128* (25), 8185–8198.
- (11) Poulos, T. L. Thirty Years of Heme Peroxidase Structural Biology. *Arch. Biochem. Biophys.* **2010**, *500* (1), 3–12.
- (12) Rodríguez-López, J. N.; Lowe, D. J.; Hernández-Ruiz, J.; Hiner, A. N. P.; García-Cánovas, F.; Thorneley, R. N. F. Mechanism of Reaction of Hydrogen Peroxide with Horseradish Peroxidase: Identification of Intermediates in the Catalytic Cycle. *J. Am. Chem. Soc.* **2001**, *123* (48), 11838–11847.
- (13) Baker, C. J.; Orlandi, E. W.; Deahl, K.; Domek, J. Scavenging of H₂O₂ and Production of Oxygen by Horseradish Peroxidase. *Arch. Biochem. Biophys.* **2000**, *382* (2), 232–237.
- (14) Hiner, A. N. P.; Hernández-Ruiz, J.; Williams, G. A.; Arnao, M. B.; García-Cánovas, F.; Acosta, M. Catalase-like Oxygen Production by Horseradish Peroxidase Must Predominantly Be an Enzyme-Catalyzed Reaction. *Arch. Biochem. Biophys.* **2001**, *392* (2), 295–302.
- (15) Campomanes, P.; Rothlisberger, U.; Alfonso-Prieto, M.; Rovira, C. The Molecular Mechanism of the Catalase-like Activity in Horseradish Peroxidase. *J. Am. Chem. Soc.* **2015**, *137* (34), 11170–11178.
- (16) Hiner, A. N. P.; Hernández-Ruiz, J.; Williams, G. A.; Arnao, M. B.; García-Cánovas, F.; Acosta, M. Catalase-like Oxygen Production by Horseradish Peroxidase Must Predominantly Be an Enzyme-Catalyzed Reaction. *Arch. Biochem. Biophys.* **2001**, *392* (2), 295–302.
- (17) Groves, J. T.; Gross, Z.; Stern, M. K. Preparation and Reactivity of Oxoiron(IV) Porphyrins. *Inorg. Chem.* **1994**, *33* (22), 5065–5072.
- (18) Dasgupta, S.; Rousseau, D. L.; Anni, H.; Yonetani, T. Structural Characterization of Cytochrome c Peroxidase by Resonance Raman Scattering. *J. Biol. Chem.* **1989**, *264* (1), 654–662.
- (19) Schappacher, M.; Weiss, R.; Montiel-Montoya, R.; Trautwein, A.; Tabard, A. Formation of an Iron(IV)-Oxo “Picket-Fence” Porphyrin Derivative via Reduction of the Ferrous Dioxxygen Adduct and Reaction with Carbon Dioxide. *J. Am. Chem. Soc.* **1985**, *107* (12), 3736–3738.
- (20) Rydberg, P.; Sigfridsson, E.; Ryde, U. On the Role of the Axial Ligand in Heme Proteins: A Theoretical Study. *J. Biol. Inorg. Chem.* **2004**, *9* (2), 203–223.
- (21) Penner-Hahn, J. E.; Smith Eble, K.; McMurry, T. J.; Renner, M.; Balch, A. L.; Groves, J. T.; Dawson, J. H.; Hodgson, K. O. Structural Characterization of Horseradish Peroxidase Using EXAFS Spectroscopy. Evidence for Fe = O Ligation in Compounds I and II. *J. Am. Chem. Soc.* **1986**, *108* (24), 7819–7825.
- (22) Penner-Hahn, J. E.; Smith Eble, K.; Dawson, J. H.; Hodgson, K. O. Structural Characterization of High Valant Intermediates in Horseradish Peroxidase. *J. Phys. Colloq.* **1986**, *47* (C8), C8-1137–C8-1142.
- (23) Myer, Y. P.; Saturno, A. F. Horse Heart Ferricytochrome c: Conformation and Heme Configuration of Low Ionic Strength Acidic Forms. *J. Protein Chem.* **1990**, *9* (4), 379–387.
- (24) Tuynman, A.; Schoemaker, H. E.; Wever, R. Enantioselective Sulfoxidations Catalyzed by Horseradish Peroxidase, Manganese Peroxidase, and Myeloperoxidase. *Monatshefte für Chemie* **2000**, *131* (6), 687–695.
- (25) Shaik, S.; Cohen, S.; de Visser, S. P.; Sharma, P. K.; Kumar, D.; Kozuch, S.; Ogliaro, F.; Danovich, D. The “Rebound Controversy”: An Overview and Theoretical Modeling of the Rebound Step in C-H Hydroxylation by Cytochrome P450. *Eur. J. Inorg. Chem.* **2004**, *2004* (2), 207–226.
- (26) Scheidt, W. R.; Reed, C. A. Spin-State/Stereochemical Relationships in Iron Porphyrins: Implications for the Hemoproteins. *Chem. Rev.* **1981**, *81* (6), 543–555.
- (27) Ogliaro, F.; Harris, N.; Cohen, S.; Filatov, M.; De Visser, S. P.; Shaik, S. A Model “rebound” Mechanism of Hydroxylation by Cytochrome P450: Stepwise and Effectively Concerted Pathways, and Their Reactivity Patterns. *J. Am. Chem. Soc.* **2000**, *122* (37), 8977–8989.
- (28) Ramdhanie, B.; Stern, C. L.; Goldberg, D. P. Synthesis of the First Corrolazine: A New Member of the Porphyrinoid Family. *J. Am. Chem. Soc.* **2001**, *123* (38), 9447–9448.
- (29) Sitter, A. J.; Reczek, C. M.; Terner, J. Heme-Linked Ionization of Horseradish Peroxidase Compound II Monitored by the Resonance Raman Fe(IV)=O Stretching Vibration. *J. Biol. Chem.* **1985**, *260* (12), 7515–7522.
- (30) La Mar, G. N.; De Ropp, J. S.; Latos-Grazynski, L.; Balch, A. L.; Johnson, R. B.; Smith, K. M.; Parish, D. W.; Cheng, R. J. Proton NMR Characterization of the Ferryl Group in Model Heme Complexes and Hemoproteins: Evidence for the FeIVO Group in Ferryl Myoglobin and Compound II of Horseradish Peroxidase. *J. Am. Chem. Soc.* **1983**, *105* (4), 782–787.
- (31) Kincaid, J. R.; Zheng, Y.; Al-Mustafa, J.; Czarnecki, K. Resonance Raman Spectra of Native and Mesoheme-Reconstituted Horseradish Peroxidase and Their Catalytic Intermediates. *J. Biol. Chem.* **1996**, *271* (46), 28805–28811.
- (32) Nilsson, K.; Hersleth, H. P.; Rod, T. H.; Andersson, K. K.; Ryde, U. The Protonation Status of Compound II in Myoglobin, Studied by a Combination of Experimental Data and Quantum Chemical Calculations: Quantum Refinement. *Biophys. J.* **2004**, *87* (5), 3437–3447.
- (33) Chance, M.; Powers, L.; Poulos, T.; Chance, B. Cytochrome c Peroxidase Compound ES Is Identical with Horseradish Peroxidase Compound I in Iron-Ligand Distances. *Biochemistry* **1986**, *25* (6), 1266–1270.
- (34) Chin, D.-H.; La Mar, G. N.; Balch, A. L. Mechanism of Autoxidation of Iron(II) Porphyrins. Detection of a Peroxo-Bridged Iron(III) Porphyrin Dimer and the Mechanism of Its Thermal Decomposition to the Oxo-Bridged Iron(III) Porphyrin Dimer. *J. Am. Chem. Soc.* **1980**, *102* (13), 4344–4350.
- (35) Hersleth, H. P.; Dalhus, B.; Görbitz, C. H.; Andersson, K. K. An Iron Hydroxide Moiety in the 1.35 Å Resolution Structure of Hydrogen Peroxide Derived Myoglobin Compound II at PH 5.2. *Journal of Biological Inorganic Chemistry* **2002**, *7* (3), 299–304.
- (36) Chance, B.; Powers, L.; Ching, Y.; Poulos, T.; Schonbaum, G. R.; Yamazaki, I.; Paul, K. G. X-Ray Absorption Studies of Intermediates in Peroxidase Activity. *Arch. Biochem. Biophys.* **1984**, *235* (2), 596–611.
- (37) Makino, R.; Uno, T.; Nishimura, Y.; Iizuka, T.; Tsuboi, M.; Ishimura, Y. Coordination Structures and Reactivities of Compound II in Iron and Manganese Horseradish Peroxidases. A Resonance Raman Study. *J. Biol. Chem.* **1986**, *261* (18), 8376–8382.
- (38) Chin, D.-H.; Balch, A. L.; La Mar, G. N. Formation of Porphyrin Ferryl (FeO₂⁺) Complexes through the Addition of Nitrogen Bases to Peroxo-Bridged Iron(III) Porphyrins. *J. Am. Chem. Soc.* **1980**, *102* (4), 1446–1448.
- (39) Green, M. T.; Dawson, J. H.; Gray, H. B. Oxoiron(IV) in Chloroperoxidase Compound II Is Basic: Implications for P450 Chemistry. *Science* **2004**, *304* (5677), 1653–1656.
- (40) Schröder, C. Proteins in Ionic Liquids: Current Status of Experiments and Simulations. *Top. Curr. Chem.* **2017**, *375* (2), 25.
- (41) Shukla, S. K.; Mikkola, J.-P. Use of Ionic Liquids in Protein and DNA Chemistry. *Front. Chem.* **2020**, *8*, 568662.
- (42) Hagen, M. L.; Harper, J. B.; Croft, A. K. Recent Advances in the Use of Ionic Liquids as Solvents for Protein-Based Materials and Chemistry. *Curr. Opin. Green Sustain. Chem.* **2022**, *36*, 100637.
- (43) Liu, Y.; Wang, M.; Li, J.; Li, Z.; He, P.; Liu, H.; Li, J. Highly Active Horseradish Peroxidase Immobilized in 1-Butyl-3-Methylimidazolium Tetrafluoroborate Room-Temperature Ionic Liquid Based Sol-Gel Host Materials. *Chem. Commun.* **2005**, *13*, 1778–1780.
- (44) Ponder, J. W.; Wu, C.; Ren, P.; Pande, V. S.; Chodera, J. D.; Schnieders, M. J.; Haque, I.; Mobley, D. L.; Lambrecht, D. S.; Distasio,

- R. A.; Head-Gordon, M.; Clark, G. N. I.; Johnson, M. E.; Head-Gordon, T. Current Status of the AMOEBA Polarizable Force Field. *J. Phys. Chem. B* **2010**, *114* (8), 2549–2564.
- (45) Shi, Y.; Xia, Z.; Zhang, J.; Best, R.; Wu, C.; Ponder, J. W.; Ren, P. Polarizable Atomic Multipole-Based AMOEBA Force Field for Proteins. *J. Chem. Theory Comput.* **2013**, *9* (9), 4046–4063.
- (46) Starovoytov, O. N.; Torabifard, H.; Cisneros, G. A. Development of AMOEBA Force Field for 1,3-Dimethylimidazolium Based Ionic Liquids. *J. Phys. Chem. B* **2014**, *118* (25), 7156–7166.
- (47) Cisneros, G. A. Application of Gaussian Electrostatic Model (GEM) Distributed Multipoles in the AMOEBA Force Field. *J. Chem. Theory Comput.* **2012**, *8* (12), 5072–5080.
- (48) Vázquez-Montelongo, E. A.; Vázquez-Cervantes, J. E.; Cisneros, G. A. Polarizable Ab Initio QM/MM Study of the Reaction Mechanism of N-Tert-Butyloxycarbonylation of Aniline in [EMIm][BF₄]. *Molecules* **2018**, *23* (11), 2830.
- (49) Søndergaard, C. R.; Olsson, M. H. M.; Rostkowski, M.; Jensen, J. H. Improved Treatment of Ligands and Coupling Effects in Empirical Calculation and Rationalization of p K_a Values. *J. Chem. Theory Comput.* **2011**, *7* (7), 2284–2295.
- (50) Olsson, M. H. M.; Søndergaard, C. R.; Rostkowski, M.; Jensen, J. H. PROPKA3: Consistent Treatment of Internal and Surface Residues in Empirical p K_a Predictions. *J. Chem. Theory Comput.* **2011**, *7* (2), 525–537.
- (51) Tu, Y.-J.; Lin, Z.; Allen, M. J.; Cisneros, G. A. Molecular Dynamics Investigation of Water-Exchange Reactions on Lanthanide Ions in Water/1-Ethyl-3-Methylimidazolium Trifluoromethylsulfate ([EMIm][OTf]). *J. Chem. Phys.* **2018**, *148* (2), 024503.
- (52) Stone, A. J. Distributed Multipole Analysis: Stability for Large Basis Sets. *J. Chem. Theory Comput.* **2005**, *1* (6), 1128–1132.
- (53) Martinez, L.; Andrade, R.; Birgin, E. G.; Martínez, J. M. PACKMOL: A Package for Building Initial Configurations for Molecular Dynamics Simulations. *J. Comput. Chem.* **2009**, *30* (13), 2157–2164.
- (54) Rackers, J. A.; Wang, Z.; Lu, C.; Laury, M. L.; Lagardère, L.; Schnieders, M. J.; Piquemal, J. P.; Ren, P.; Ponder, J. W. Tinker 8: Software Tools for Molecular Design. *J. Chem. Theory Comput.* **2018**, *14* (10), 5273–5289.
- (55) Petersen, H. G. Accuracy and Efficiency of the Particle Mesh Ewald Method. *J. Chem. Phys.* **1995**, *103* (9), 3668–3679.
- (56) Darden, T.; York, D.; Pedersen, L. Particle Mesh Ewald: An N-log(N) Method for Ewald Sums in Large Systems. *J. Chem. Phys.* **1993**, *98* (12), 10089–10092.
- (57) Essmann, U.; Perera, L.; Berkowitz, M. L.; Darden, T.; Lee, H.; Pedersen, L. G. A Smooth Particle Mesh Ewald Method. *J. Chem. Phys.* **1995**, *103* (19), 8577–8593.
- (58) Steinbach, P. J.; Brooks, B. R. New Spherical-cutoff Methods for Long-range Forces in Macromolecular Simulation. *J. Comput. Chem.* **1994**, *15* (7), 667–683.
- (59) Bussi, G.; Zykova-Timan, T.; Parrinello, M. Isothermal-Isobaric Molecular Dynamics Using Stochastic Velocity Rescaling. *J. Chem. Phys.* **2009**, *130* (7), 74101.
- (60) Berendsen, H. J. C.; Postma, J. P. M.; Van Gunsteren, W. F.; Dinola, A.; Haak, J. R. Molecular Dynamics with Coupling to an External Bath. *J. Chem. Phys.* **1984**, *81* (8), 3684–3690.
- (61) Humphrey, W.; Dalke, A.; Schulten, K. VMD: Visual Molecular Dynamics. *J. Mol. Graph.* **1996**, *14* (1), 33–38.
- (62) (a) Michaud-Agrawal, N.; Denning, E. J.; Woolf, T. B.; Beckstein, O. MDAnalysis: A Toolkit for the Analysis of Molecular Dynamics Simulations. *J. Comput. Chem.* **2011**, *32* (10), 2319–2327. (b) Gowers, R. J.; Linke, M.; Barnoud, J.; Reddy, T. J. E.; Melo, M. N.; Seyler, S. L.; Domański, J.; Dotson, D. L.; Buchoux, S.; Kenney, I. M.; Beckstein, O. MDAnalysis: A Python Package for the Rapid Analysis of Molecular Dynamics Simulations. In *Proceedings of the 15th Python in Science Conference*; Bentham, S.; Rostrup, S., Eds.; SciPy, 2016; pp 98–105.
- (63) Michaud-Agrawal, N.; Denning, E. J.; Woolf, T. B.; Beckstein, O. MDAnalysis: A Toolkit for the Analysis of Molecular Dynamics Simulations. *J. Comput. Chem.* **2011**, *32* (10), 2319–2327.
- (64) Brehm, M.; Kirchner, B. TRAVIS - A Free Analyzer and Visualizer for Monte Carlo and Molecular Dynamics Trajectories. *J. Chem. Inf. Model.* **2011**, *51* (8), 2007–2023.
- (65) Brehm, M.; Thomas, M.; Gehrke, S.; Kirchner, B. TRAVIS—A Free Analyzer for Trajectories from Molecular Simulation. *J. Chem. Phys.* **2020**, *152* (16), 164105.
- (66) Brehm, M.; Kirchner, B. TRAVIS - A Free Analyzer and Visualizer for Monte Carlo and Molecular Dynamics Trajectories. *J. Chem. Inf. Model.* **2011**, *51* (8), 2007–2023.
- (67) Hollóczki, O.; Macchiagodena, M.; Weber, H.; Thomas, M.; Brehm, M.; Stark, A.; Russina, O.; Triolo, A.; Kirchner, B. Triphilic Ionic-Liquid Mixtures: Fluorinated and Non-Fluorinated Aprotic Ionic-Liquid Mixtures. *ChemPhysChem* **2015**, *16* (15), 3325–3333.
- (68) Pedregosa, F.; Varoquaux, G.; Gramfort, A.; Michel, V.; Thirion, B.; Grisel, O.; Blondel, M.; Prettenhofer, P.; Weiss, R.; Dubourg, V.; Vanderplas, J.; Passos, A.; Cournapeau, D.; Brucher, M.; Perrot, M.; Duchesnay, E. Scikit-Learn: Machine Learning in Python. *J. Mach. Learn. Res.* **2011**, *12*, 2825–2830.
- (69) Gökcen, H.; Vázquez-Montelongo, E. A.; Cisneros, G. A. LICHEM 1.1: Recent Improvements and New Capabilities. *J. Chem. Theory Comput.* **2019**, *15* (5), 3056–3065.
- (70) Kratz, E. G.; Walker, A. R.; Lagardère, L.; Lipparini, F.; Piquemal, J. P.; Andrés Cisneros, G. LICHEM: A QM/MM Program for Simulations with Multipolar and Polarizable Force Fields. *J. Comput. Chem.* **2016**, *37* (11), 1019–1029.
- (71) Nochebuena, J.; Naseem-Khan, S.; Cisneros, G. A. Development and Application of Quantum Mechanics/Molecular Mechanics Methods with Advanced Polarizable Potentials. *WIREs Comput. Mol. Sci.* **2021**, *11* (4), No. e1515.
- (72) Ren, P.; Ponder, J. W. Polarizable Atomic Multipole Water Model for Molecular Mechanics Simulation. *J. Phys. Chem. B* **2003**, *107* (24), 5933–5947.
- (73) Ren, P.; Wu, C.; Ponder, J. W. Polarizable Atomic Multipole-Based Molecular Mechanics for Organic Molecules. *J. Chem. Theory Comput.* **2011**, *7* (10), 3143–3161.
- (74) Shi, Y.; Xia, Z.; Zhang, J.; Best, R.; Wu, C.; Ponder, J. W.; Ren, P. Polarizable Atomic Multipole-Based AMOEBA Force Field for Proteins. *J. Chem. Theory Comput.* **2013**, *9* (9), 4046–4063.
- (75) Ponder, J. W.; Wu, C.; Ren, P.; Pande, V. S.; Chodera, J. D.; Schnieders, M. J.; Haque, I.; Mobley, D. L.; Lambrecht, D. S.; Distasio, R. A.; Head-Gordon, M.; Clark, G. N. I.; Johnson, M. E.; Head-Gordon, T. Current Status of the AMOEBA Polarizable Force Field. *J. Phys. Chem. B* **2010**, *114* (8), 2549–2564.
- (76) Pappu, R. V.; Hart, R. K.; Ponder, J. W. Analysis and Application of Potential Energy Smoothing and Search Methods for Global Optimization. *J. Phys. Chem. B* **1998**, *102* (48), 9725–9742.
- (77) Ponder, J. W.; Richards, F. M. An Efficient Newton-like Method for Molecular Mechanics Energy Minimization of Large Molecules. *J. Comput. Chem.* **1987**, *8* (7), 1016–1024.
- (78) Kundrot, C. E.; Ponder, J. W.; Richards, F. M. Algorithms for Calculating Excluded Volume and Its Derivatives as a Function of Molecular Conformation and Their Use in Energy Minimization. *J. Comput. Chem.* **1991**, *12* (3), 402–409.
- (79) Davidon, W. C. Variable Metric Method for Minimization. *SIAM J. Optim.* **1991**, *1* (1), 1–17.
- (80) Fletcher, R.; Powell, M. J. D. A Rapidly Convergent Descent Method for Minimization. *Comput. J.* **1963**, *6* (2), 163–168.
- (81) Burger, S. K.; Yang, W. Quadratic String Method for Determining the Minimum-Energy Path Based on Multiobjective Optimization. *J. Chem. Phys.* **2006**, *124* (5), 54109.
- (82) Śmiga, S.; Constantin, L. A. Unveiling the Physics behind Hybrid Functionals. *J. Phys. Chem. A* **2020**, *124* (27), 5606–5614.
- (83) Adamo, C.; Barone, V. Toward Reliable Density Functional Methods without Adjustable Parameters: The PBE0 Model. *J. Chem. Phys.* **1999**, *110* (13), 6158–6170.
- (84) Perdew, J. P.; Ernzerhof, M.; Burke, K. Rationale for Mixing Exact Exchange with Density Functional Approximations. *J. Chem. Phys.* **1996**, *105* (22), 9982–9985.

- (85) Hehre, W. J.; Ditchfield, K.; Pople, J. A. Self-Consistent Molecular Orbital Methods. XII. Further Extensions of Gaussian-Type Basis Sets for Use in Molecular Orbital Studies of Organic Molecules. *J. Chem. Phys.* **1972**, *56* (5), 2257–2261.
- (86) Ditchfield, R.; Hehre, W. J.; Pople, J. A. Self-Consistent Molecular-Orbital Methods. IX. An Extended Gaussian-Type Basis for Molecular-Orbital Studies of Organic Molecules. *J. Chem. Phys.* **1971**, *54* (2), 724–728.
- (87) Clark, T.; Chandrasekhar, J.; Spitznagel, G. W.; Schleyer, P. V. R. Efficient Diffuse Function-augmented Basis Sets for Anion Calculations. III. The 3-21+G Basis Set for First-row Elements, Li-F. *J. Comput. Chem.* **1983**, *4* (3), 294–301.
- (88) Weigend, F.; Ahlrichs, R. Balanced Basis Sets of Split Valence, Triple Zeta Valence and Quadruple Zeta Valence Quality for H to Rn: Design and Assessment of Accuracy. *Phys. Chem. Chem. Phys.* **2005**, *7* (18), 3297–3305.
- (89) Rydberg, P.; Olsen, L. The Accuracy of Geometries for Iron Porphyrin Complexes from Density Functional Theory. *J. Phys. Chem. A* **2009**, *113* (43), 11949–11953.
- (90) Chaudret, R.; Parks, J. M.; Yang, W. Pseudobond Parameters for QM/MM Studies Involving Nucleosides, Nucleotides, and Their Analogs. *J. Chem. Phys.* **2013**, *138* (4), 45102.
- (91) Parks, J. M.; Hu, H.; Cohen, A. J.; Yang, W. A Pseudobond Parametrization for Improved Electrostatics in Quantum Mechanical/Molecular Mechanical Simulations of Enzymes. *J. Chem. Phys.* **2008**, *129* (15), 154106.
- (92) Lewin, J. L.; Cramer, C. J. Modified Carbon Pseudopotential for Use in ONIOM Calculations of Alkyl-Substituted Metallocenes. *J. Phys. Chem. A* **2008**, *112* (50), 12754–12760.
- (93) Xiao, C.; Zhang, Y. Design-Atom Approach for the Quantum Mechanical/Molecular Mechanical Covalent Boundary: A Design-Carbon Atom with Five Valence Electrons. *J. Chem. Phys.* **2007**, *127* (12), 124102.
- (94) Zhang, Y.; Lee, T. S.; Yang, W. A Pseudobond Approach to Combining Quantum Mechanical and Molecular Mechanical Methods. *J. Chem. Phys.* **1999**, *110* (1), 46–54.
- (95) Kratz, E. G.; Duke, R. E.; Cisneros, G. A. Long-Range Electrostatic Corrections in Multipolar/Polarizable QM/MM Simulations. *Theor. Chem. Acc.* **2016**, *135* (7), 166.
- (96) Fang, D.; Duke, R. E.; Cisneros, G. A. A New Smoothing Function to Introduce Long-Range Electrostatic Effects in QM/MM Calculations. *J. Chem. Phys.* **2015**, *143* (4), 44103.
- (97) Lu, T.; Chen, F. Multiwfn: A Multifunctional Wavefunction Analyzer. *J. Comput. Chem.* **2012**, *33* (5), 580–592.
- (98) Johnson, E. R.; Keinan, S.; Mori-Sánchez, P.; Contreras-García, J.; Cohen, A. J.; Yang, W. Revealing Noncovalent Interactions. *J. Am. Chem. Soc.* **2010**, *132* (18), 6498–6506.
- (99) Ito, T.; Harada, S.; Homma, H.; Okabe, A.; Nemoto, T. Mechanistic Investigation on Dearomatic Spirocyclization of Arenes with α -Diazoamide under Boron Catalysis. *ACS Catal.* **2023**, *13* (1), 147–157.
- (100) Contreras-García, J.; Johnson, E. R.; Keinan, S.; Chaudret, R.; Piquemal, J. P.; Beratan, D. N.; Yang, W. NCIPILOT: A Program for Plotting Noncovalent Interaction Regions. *J. Chem. Theory Comput.* **2011**, *7* (3), 625–632.
- (101) Maghsoud, Y.; Dong, C.; Cisneros, G. A. Investigation of the Inhibition Mechanism of Xanthine Oxidoreductase by Oxitipurinol: A Computational Study. *J. Chem. Inf. Model.* **2023**, *63* (13), 4190–4206.
- (102) Walker, M. G.; Mendez, C. G.; Ho, P. S. Non-Classical Non-Covalent σ -Hole Interactions in Protein Structure and Function: Concepts for Potential Protein Engineering Applications. *Chem.—Asian J.* **2023**, *18* (7), No. e202300026.
- (103) Johnson, E. R.; Keinan, S.; Mori-Sánchez, P.; Contreras-García, J.; Cohen, A. J.; Yang, W. Revealing Noncovalent Interactions. *J. Am. Chem. Soc.* **2010**, *132* (18), 6498–6506.
- (104) Savin, A.; Silvi, B.; Colonna, F. Topological Analysis of the Electron Localization Function Applied to Delocalized Bonds. *Can. J. Chem.* **1996**, *74*, 1088–1096.
- (105) Savin, A. On the Significance of ELF Basins. *J. Chem. Sci.* **2005**, *117* (5), 473–475.
- (106) Thom, A. J. W.; Sundstrom, E. J.; Head-Gordon, M. LOBA: A Localized Orbital Bonding Analysis to Calculate Oxidation States, with Application to a Model Water Oxidation Catalyst. *Phys. Chem. Chem. Phys.* **2009**, *11* (47), 11297–11304.
- (107) Chai, J.-D.; Head-Gordon, M. Systematic Optimization of Long-Range Corrected Hybrid Density Functionals. *J. Chem. Phys.* **2008**, *128* (8), 084106.
- (108) Chai, J. Da; Head-Gordon, M. Long-Range Corrected Hybrid Density Functionals with Damped Atom-Atom Dispersion Corrections. *Phys. Chem. Chem. Phys.* **2008**, *10* (44), 6615–6620.